Research Article Vol. 28, No. 4 / 17 February 2020 / Optics Express 5257
Optics EXPRESS

Extreme ultraviolet lensless imaging without object support through rotational diversity in diffractive shearing interferometry

A. C. C. DE BEURS,[1,2,6] X. LIU,[1,2] G. S. M. JANSEN,[1,2,3] A. P. KONIJNENBERG,[4,5] W. M. J. COENE,[4,5] K. S. E. EIKEMA,[1,2] AND S. WITTE[1,2,7]

[1]*Advanced Research Center for Nanolithography (ARCNL), Science Park 106, 1098 XG Amsterdam, The Netherlands*
[2]*Department of Physics and Astronomy, and LaserLaB, Vrije Universiteit, De Boelelaan 1081, 1081 HV Amsterdam, The Netherlands*
[3]*Present address: Georg-August University Göttingen, 37073 Göttingen, Germany*
[4]*Optics Research Group, Delft University of Technology, Delft 2628 CH, The Netherlands*
[5]*ASML Netherlands B.V., De Run 6501, 5504 DR Veldhoven, The Netherlands*
[6]*beurs@arcnl.nl*
[7]*witte@arcnl.nl*

Abstract: We report on a method that allows microscopic image reconstruction from extreme-ultraviolet diffraction patterns without the need for object support constraints or other prior knowledge about the object structure. This is achieved by introducing additional diversity through rotation of an object in a rotationally asymmetric probe beam, produced by the spatial interference between two phase-coherent high-harmonic beams. With this rotational diffractive shearing interferometry method, we demonstrate robust image reconstruction of microscopic objects at wavelengths around 30 nm, using images recorded at only three to five different object rotations.

1. Introduction

In recent years, coherent diffractive imaging (CDI) has proved to be a versatile imaging technique with many applications, such as high-resolution imaging using X-ray and extreme ultraviolet (XUV) [1–4] as well as coherent beams of electrons [5] as illumination. High harmonic generation (HHG) is a process that enabled the development of tabletop sources generating a broad harmonic spectrum of spatially coherent XUV light [6]. Using these sources recently sub-wavelength resolution has been achieved [7]. The broad bandwidth of HHG sources enables imaging over wide wavelength spans throughout the extreme ultraviolet and soft-X-ray ranges. Recently we have demonstrated multi-wavelength CDI based on Fourier-transform spectroscopy [8,9], and various promising spectrally resolved imaging results have been reported [10,11].

In CDI, the exit wave of an object is reconstructed from a measured diffraction intensity pattern. In the far-field limit, the diffracted electric field corresponds to the Fourier-transform of the exit wave. Therefore, a reconstruction of this exit wave can be obtained by an inverse Fourier-transform of this diffracted electric field. The challenge in CDI measurements is that typically only the squared amplitude of this electric field is measured. To reconstruct the exit wave, the phase of the electric field at the detector plane needs to be retrieved using iterative methods [12,13]. In the single-shot implementation of CDI, such algorithms rely on additional information, which often means knowledge of the object support. Finding a good estimate of such a support is often difficult, and can be solved in a number of ways: By using low resolution microscopy technique, such as optical microscopy [12] or Fourier-transform holography [14]. Another commonly used technique is shrinkwrap [15], where the object support is adaptively refined from a loose starting

#380056 https://doi.org/10.1364/OE.380056
Journal © 2020 Received 11 Oct 2019; revised 31 Jan 2020; accepted 2 Feb 2020; published 11 Feb 2020

Optics EXPRESS

guess of the support. However, for objects with non-sharp edges, shrinkwrap-based algorithms require the user to make a choice about the threshold value at which to define the support boundary. Many recent developments have been driven by ptychography [11,16,17]. Ptychography uses transverse scanning of a spatially confined probe beam, while maintaining partial overlap between adjacent scan positions. This approach introduces additional translational measurement diversity which strongly constrains the exit wave solution. Ptychographic methods remove the need for an object support and the associated prior object knowledge, and simultaneously provide a reconstruction of the probe beam [17], but it does come at the cost of a strongly increased number of measurements.

In this paper, we present a novel approach to CDI that enables high-resolution imaging without the need for an object support in the reconstruction algorithm, using only a limited number of measurements with a rotating interference pattern as the probe. Our approach is based on the diffractive shearing interferometry (DSI) approach which allows wavelength-resolved CDI. For our present application we use XUV radiation generated by HHG [18]. In DSI, the interference between two sheared diffraction patterns is measured through spatially resolved Fourier-transform spectroscopy (FTS) [8]. Effectively, this provides a measure of the phase gradient in the direction of the shear [19]. We now extend this approach by measuring multiple shear directions. In analogy to ptychography, these multiple measurements provide increased measurement diversity since our interferometric illumination is rotationally asymmetric. A phase retrieval approach that rotates an asymmetric illumination was earlier suggested by Wang et al. [20], and we recently explored the concept of interferometric probe ptychography in detail for visible light applications [21]. Shearing interferometry methods for phase imaging with visible light [22], deep-UV [23] and X-rays [24] have also been reported. Here we show that the obtained diffraction information is sufficient to accurately reconstruct an object image without the need for accurate knowledge of an object support. The only requirements are 1) that the diffraction pattern is sufficiently sampled, meaning that the object is fully contained within the field of view, and 2) that the illumination is smooth across the object (as is the case for CDI in general). The experimental results are further supported by numerical simulations, in which the influence of the number of orientations, the relative magnitude of the shear and the signal-to-noise ratio are investigated.

2. Rotational diffractive shearing interferometry

The measurement concept is shown in Fig. 1. An object is illuminated by a pair of broadband noncollinear HHG beams, which are produced using phase-locked pairs of intense driving laser pulses [18]. The noncollinear geometry gives rise to a coherent, spatially sheared pair of diffraction patterns at a camera placed in the far field. A series of far-field diffraction patterns is recorded as a function of the time delay between the HHG pulses. The combination of such sheared illumination with an FTS scan enables spectrally resolved diffractive imaging for the different harmonic wavelengths through diffractive shearing interferometry (DSI) [8]. Note that in the direction opposite to the shearing direction, extra support information is still required. To remove the need for such support information, the object is rotated and DSI diffraction data is recorded for a series of object angles, while the shear between the two beams remains fixed. In this section, this rotational DSI approach is explained in detail, and the phase retrieval algorithm required for image reconstruction is outlined.

2.1. Diffractive shearing interferometry

With DSI combined with FTS, it is possible to recover two identical but laterally sheared monochromatic diffraction-plane electric fields from their interference [8]. FTS scans provide (after Fourier transformation with respect to the time delay between the two pulses) such a signal

Optics EXPRESS

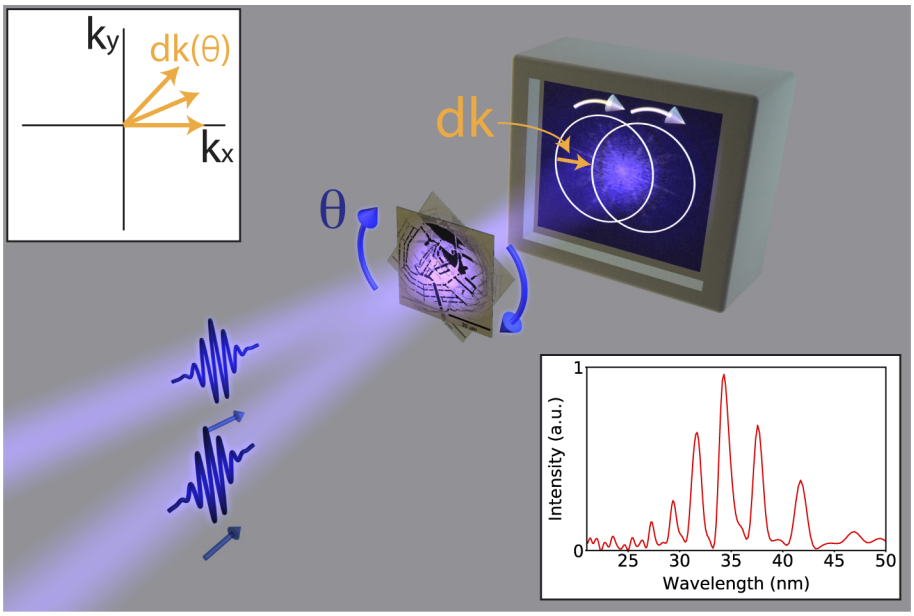

Fig. 1. Two mutually delayed, identical XUV beams are incident on our sample in a non-collinear geometry. The signal measured on the camera is the interference pattern between two laterally sheared diffraction patterns. A time delay (FTS) scan is recorded for a range of sample rotations along angle θ, which introduces measurement diversity because of the directed interference in the illumination. The top left inset depicts how the relative shear vector $\boldsymbol{dk}$ changes in k-space upon sample rotation. The amplitude of $\boldsymbol{dk}$ is exaggerated for clarity. The bottom right inset shows a typical HHG spectrum retrieved from an FTS scan.

resolved for each wavelength of the light source:

$$\begin{aligned} M(\boldsymbol{k}) &= E(\boldsymbol{k}+\boldsymbol{dk})E(\boldsymbol{k}-\boldsymbol{dk})^* \\ &= A(\boldsymbol{k}+\boldsymbol{dk})A(\boldsymbol{k}-\boldsymbol{dk})\exp\{i(\Phi(\boldsymbol{k}+\boldsymbol{dk})-\Phi(\boldsymbol{k}-\boldsymbol{dk})]\}, \end{aligned} \tag{1}$$

where the measured signal $M(\boldsymbol{k})$ corresponds to the product of the diffracted electric field $E(\boldsymbol{k}+\boldsymbol{dk})$ and its complex conjugate with opposite shear $E(\boldsymbol{k}-\boldsymbol{dk})^*$. $A(\boldsymbol{k})$ is the amplitude of the electric field of a single beam at the camera and $\Phi(\boldsymbol{k})$ is the phase of the electric field, $\boldsymbol{k}$ are the camera plane coordinates and $2\boldsymbol{dk}$ is the combined lateral shear between the two beams. Note that bold-font symbols are used to indicate vectors. As can be seen from Eq. (1), the retrieved diffraction data does not directly correspond to the far-field diffraction pattern of the object, as the complex product between the two beams is measured instead of the intensity. An advantage of this measurement is that the complex phase term provides information about the spatial phase derivative along the direction of the shear between the beams.

Starting from $M(\mathbf{k})$ it is possible to reconstruct the full complex far-field electric field of a single illumination beam, which is related to the object exit wave by a spatial Fourier-transform. This can be achieved by using an iterative phase retrieval algorithm [13,25], which combines a finite support constraint with a camera space electric field update that takes into account the sheared geometry:

$$E_{n+1}(\boldsymbol{k}) = (1-\beta)E_n(\boldsymbol{k}) + \frac{\beta}{2}\left[\frac{M(\boldsymbol{k}-\boldsymbol{dk})E_n(\boldsymbol{k}-2\boldsymbol{dk})}{|E_n(\boldsymbol{k}-2\boldsymbol{dk})|^2+\alpha^2} + \frac{M^*(\boldsymbol{k}+\boldsymbol{dk})E_n(\boldsymbol{k}+2\boldsymbol{dk})}{|E_n(\boldsymbol{k}+2\boldsymbol{dk})|^2+\alpha^2}\right], \tag{2}$$

Optics EXPRESS

where E_n is the n^{th} update step of the electric field estimate, β is a feedback parameter with a value close to unity that prevents amplitude overshooting, and α is a regularization constant to avoid division by zero.

2.2. Rotational diffractive shearing interferometry

As shown in Fig. 1, the rotational symmetry that would be present for single-beam illumination is broken by the fixed shear direction in the noncollinear double-beam illumination. Therefore, rotating the object around the average beam axis results in a qualitatively different diffraction pattern at the detector, as the individual diffraction patterns rotate but the interference direction remains fixed. Measurements at multiple rotation angles therefore provide increased measurement diversity. This additional information forms the basis for a phase retrieval algorithm that does not require support constraints or other prior sample-plane knowledge. Instead, it suffices to impose a constraint that requires the single-beam electric fields measured at different shear angles, as retrieved from a DSI procedure, to be identical. Because of the experimental challenge involved in rotating the shear direction between two HHG beams, we choose to rotate the object around an axis given by the average beam direction (Fig. 1). A series of DSI measurements is then performed as a function of this rotation angle. After the measurement, the resulting datasets are numerically rotated so that effectively the respective complex fields are acquired at different orientations of the object relative to a common orientation. This procedure is equivalent to the measurement of DSI patterns with a rotating shear. To accurately perform this numerical rotation of complex field data sampled on a square grid, a method is used that synthesises rotations by using a set of three shear operations [26]. This rotated data forms the starting point for an augmented DSI algorithm, which begins with a starting guess for the unsheared electric field $E_{0,j}(\boldsymbol{k})$ for each measurement j at shear angle θ_j. The unsheared electric fields are then updated using the standard DSI camera space update [8], but now for each angle θ_j:

$$E_{n+1,j}(\boldsymbol{k}) = (1-\beta)E_n(\boldsymbol{k}) + \frac{\beta}{2}\left[\frac{M_j(\boldsymbol{k}-\boldsymbol{dk_j})E_n(\boldsymbol{k}-2\boldsymbol{dk_j})}{|E_n(\boldsymbol{k}-2\boldsymbol{dk_j})|^2+\alpha^2} + \frac{M_j^*(\boldsymbol{k}+\boldsymbol{dk_j})E_n(\boldsymbol{k}+2\boldsymbol{dk_j})}{|E_n(\boldsymbol{k}+2\boldsymbol{dk_j})|^2+\alpha^2}\right], \tag{3}$$

where $M_j(\boldsymbol{k})$ is the measured signal at θ_j, $E_{n,j}(\boldsymbol{k})$ is the current field reconstruction and at that angle. Note that we refer to our camera-space coordinates as $\boldsymbol{k}$, since the camera plane takes the role of reciprocal space in our measurements. After each update, the field reconstructions in the object plane for all angles are averaged to obtain the field estimate for the next iteration:

$$E_{n+1}(\boldsymbol{r}) = \langle E_{n+1,j}(\boldsymbol{r})\rangle \tag{4}$$

While the algorithm typically converges for both simulated and experimental data, it was observed that on several occasions the convergence stagnated in a local minimum. A probable cause for this stagnation is the presence of a possible relative phase shift between the sheared diffraction patterns retrieved at different angles, which can lead to errors in the field average in Eq. (4). This relative phase offset is challenging to retrieve from the iterative procedure directly. Therefore, to aid reconstruction and further improve the algorithm convergence properties we instead apply an additional constraint in the averaging step, typically after every 40 iterations:

$$E_{n+1}(\boldsymbol{r}) = \gamma\langle|E_{n+1,j}(\boldsymbol{r})|\rangle + (1-\gamma)E_n(\boldsymbol{r}) \tag{5}$$

This constraint has the effect of damping object phase variations, and is therefore similar to a positivity constraint. However, it is not as strict as a true positivity constraint because of the introduction of the relaxation parameter γ. The value of γ is typically around 0.5.

Optics EXPRESS

3. Numerical simulations of rotational DSI

To systematically investigate how the quality of the reconstructions depends on the number of measurements at different rotation angles, we have performed a series of numerical simulations. The results of these simulations is shown in Fig. 2. Starting out from a test image (Fig. 2(a)), we simulate multiple DSI patterns for a range of different shear vector angles. In the simulations, the angle of the shear vector is rotated instead of the object, so that numerical object rotation of the diffraction data is not needed. Care is taken to simulate the far-field DSI patterns with a signal-to-noise ratio (SNR) comparable to our experimental data, which will be discussed in Section 4. The intensity and phase of a typical simulated DSI pattern are shown in Figs. 2(b) and 2(c). We typically choose the magnitude of the shear to be around 5 pixels, which is slightly larger than the typical speckle size of the diffraction patters, as this was previously found to give the best DSI reconstructions [8]. A series of DSI patterns is generated with the shear rotated to angles of $0°, 10°, 15°, 80°$ and $90°$, respectively. The same angles were used to obtain the experimental results, which will be discussed below. Reconstructions are then performed

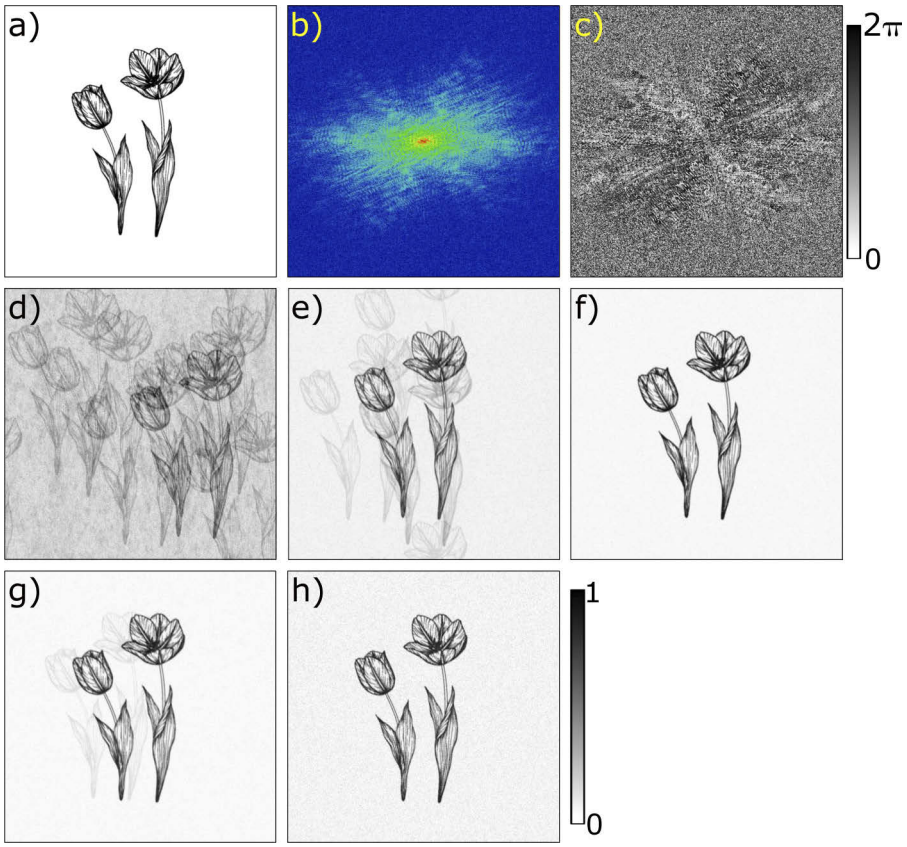

Fig. 2. Numerical simulations of the algorithm performance as a function of number of included measurement angles. (a) Intensity image of the simulated object (a flat phase is assumed) (b, c) Far-field DSI intensity (b) and phase (c) pattern as they would be recorded in an experiment. (d-g) Reconstructed images of the object when including data respectively from two, three, four and five measurements recorded at different angles . Each of these images is the average of 10 independent reconstructions. (h) Typical result for a single reconstruction, using diffraction signals at five different shear angles. The colorbar bar right of (h) applies to all intensity images of the object.

Optics EXPRESS

using subsets of these DSI patterns, for an increasing number of angles ranging from two to five. These subsets always included the 0° and 90° datasets, because this pair introduces the largest diversity due to the orthogonal shears. The other angles were selected randomly in each subset. For each of these subsets, ten independent reconstructions were performed using randomized starting field guesses and shear orientations. Of these ten reconstructions, the average is then taken as the overall reconstruction result for the subset corresponding to that particular number of shear angles. These averaged reconstruction results are shown in Figs. 2(d)–2(g). In these reconstructions, the total number of camera update steps (Eq. (3)) was kept constant.

It was found that when using only two shear angles, convergence was not guaranteed, and the reconstruction quality varied as a function of both the direction of the shear and the starting guess of the electric field. In the cases for which the algorithm did converge, it would often converge to a solution in a step-like manner after showing no visible improvement for many iterations, as illustrated in Fig. 3(a). Figure 3 shows the normalised mean square error (NMSE) [27] as a function of the number of iterations. This NMSE is given by the expression:

$$Error = \sqrt{\frac{\sum_{\boldsymbol{k},j} |M_j(\boldsymbol{k}) - M_{rec,j}(\boldsymbol{k})|^2}{\sum_{\boldsymbol{k},j} |M_{rec,j}(\boldsymbol{k})|^2}} \tag{6}$$

where $M_{rec,j}$ and M_j are the reconstructed and measured interference terms, respectively. For the simulated datasets consisting of DSI patterns for three to five shear angles, the algorithm reliably converged to a clearly recognizable object image. From the averaged data (Figs. 2(e)–2(g)), it does become clear that there is some remaining variability in the exact position of the object in the transverse plane. This effect is significant for three angles, but strongly reduces for four and five angles. For comparison, a single (non-averaged) reconstruction result when taking five angles into account is displayed in Fig. 2(h). This improved convergence behaviour is also apparent in Fig. 3(b), which shows the NMSE for a reconstruction including five angles. Compared to the two-angle reconstruction, convergence is much faster and less erratic, and proceeds in a nearly monotonous fashion. Note that the periodic spikes in the NMSE for the five-angle reconstruction stem from the application of the update constraint Eq. (5) every 40$^{\text{th}}$ iteration. From the reconstructed images and the error metric, the five-angle case is found to converge after just 70-100 iterations, after which the error metric only shows such periodic behaviour due to the regular update constraint application discussed above. In contrast, the spiking behaviour in the two-angle NMSE is irregular and cannot fully be explained by this constraint application.

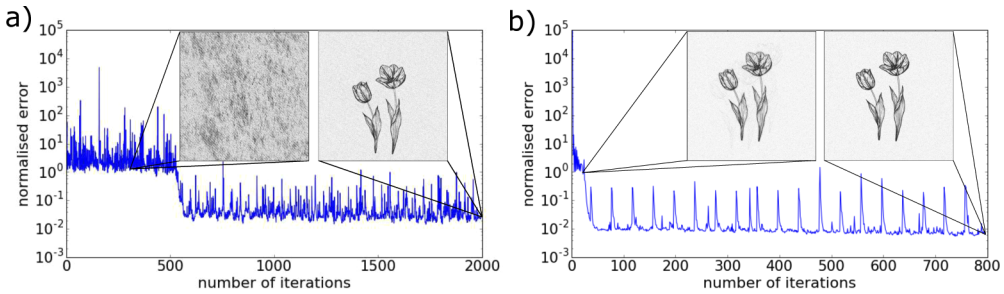

Fig. 3. Estimation of convergence, using the normalised mean square error metric (Eq. (6)) as a function of the number of iterations for a simulation with (a) two and (b) five diffraction patterns with varying shear-object orientations. The insets show reconstructed images after different amounts of iterations.

Optics EXPRESS

4. Experimental demonstration of rotational DSI

4.1. Setup and measurement procedure for DSI with a HHG source

To experimentally demonstrate the concept of rotational diversity in DSI, a series of measurements was performed in an XUV lensless imaging geometry. The XUV radiation is produced by focusing 1 mJ, 25 fs laser pulses at a central wavelength of 800 nm from an optical parametric chirped pulse amplifier into a jet of Argon gas. The beam is focused with an f = 25 cm plano-convex lens. The gas jet is 1 mm wide, and produced by a pulsed nozzle backed by up to 8 bar of Argon that ejects gas into a metal tube to constrain the flow. The laser intersects the jet through small holes in the side of the metal tube. The repetition rate of the laser system is 300 Hz. To enable spectrally resolved imaging we use an FTS-approach. A coherent pair of HHG pulses is produced by two phase-stable driving laser pulses, which each focus in a separate location inside the gas jet but interfere at the object location. Further details of this method are given in previous work [8,18]. A typical HHG spectrum as used in this experiment is shown in Fig. 1.

The object under study is a transmission sample, representing a map of the water ways in the city of Amsterdam, manufactured using focused ion beam milling. The object substrate consists of a freestanding 50 nm thick silicon nitride film, coated on both sides with 70 nm of gold. A scanning electron microscope (SEM) image of the object is shown in Fig. 4(a). In the black areas in this image, the film was fully milled through, while in some parts the material was only partially removed, so that the object should appear as a 'grayscale' intensity image under XUV exposure.

The sample is placed at a distance of 18 cm from the detector (Andor Ikon-L, 2048×2048 pixels, 13.5 μm pixel size). The lateral shear between the two diffraction patterns at the detector plane is set to 134 μm, corresponding to about 10 pixels and an angle of 67 μrad. The rotation of the sample with respect to the shear direction (angle θ in Fig. 1) is controlled by a piezo-driven rotation stage. FTS scans were performed for a series of angles, being 0°, 10°, 15°, 80° and 90°, respectively. These particular angles were selected to minimize the error in the numerical rotation of the diffraction patterns. For the FTS scan at 0°, a time scan of 6.2 fs is recorded in steps of 34.4 attoseconds. These scan parameters correspond to a Nyquist-sampled spectral range of 14.5 PHz sampled at a frequency spacing of 164 THz. For the measurements at the other angles, a time scan of 6.3 fs was recorded in slightly larger time steps of 42.2 attoseconds, which results in a similar frequency spacing but at a somewhat smaller spectral range of 11.9 PHz. Each diffraction pattern in the FTS scans consists of set of exposures of 10 s, 2 s and 0.5 s, which are numerically merged into one image with increased dynamic range. We emphasize that the large number of images recorded in this measurement is specific for our Fourier-transform approach to diffractive imaging [9], and provides diffraction patterns for all wavelengths in the HHG source spectrum simultaneously. When instead using spectral filtering before the sample, the rotational DSI approach presented here in principle only requires a two to four recordings at different phase steps for each angle, which can be obtained in a total measurement time of a few minutes.

4.2. Measurement results and rotational DSI reconstructions

DSI signals at a wavelength of 31 nm as obtained from the FTS scan are shown in Fig. 4(b)–4(g). From these diffraction patterns, object reconstructions are performed using the rotational DSI procedure described in Section 2.2. Reconstructions are attempted using the data from a varying number of angles ranging from two to five, similar to what was done for the simulations described in the previous section. For all reconstructions, the total number of algorithm iterations was kept fixed at 3000 for all reconstructions.

For the experimental data, very similar convergence behaviour was observed compared to the simulations. When using two angles, the algorithm generally did not converge reliably. When including data from three to five angles, convergence was much more robust and proceeded in

Optics EXPRESS

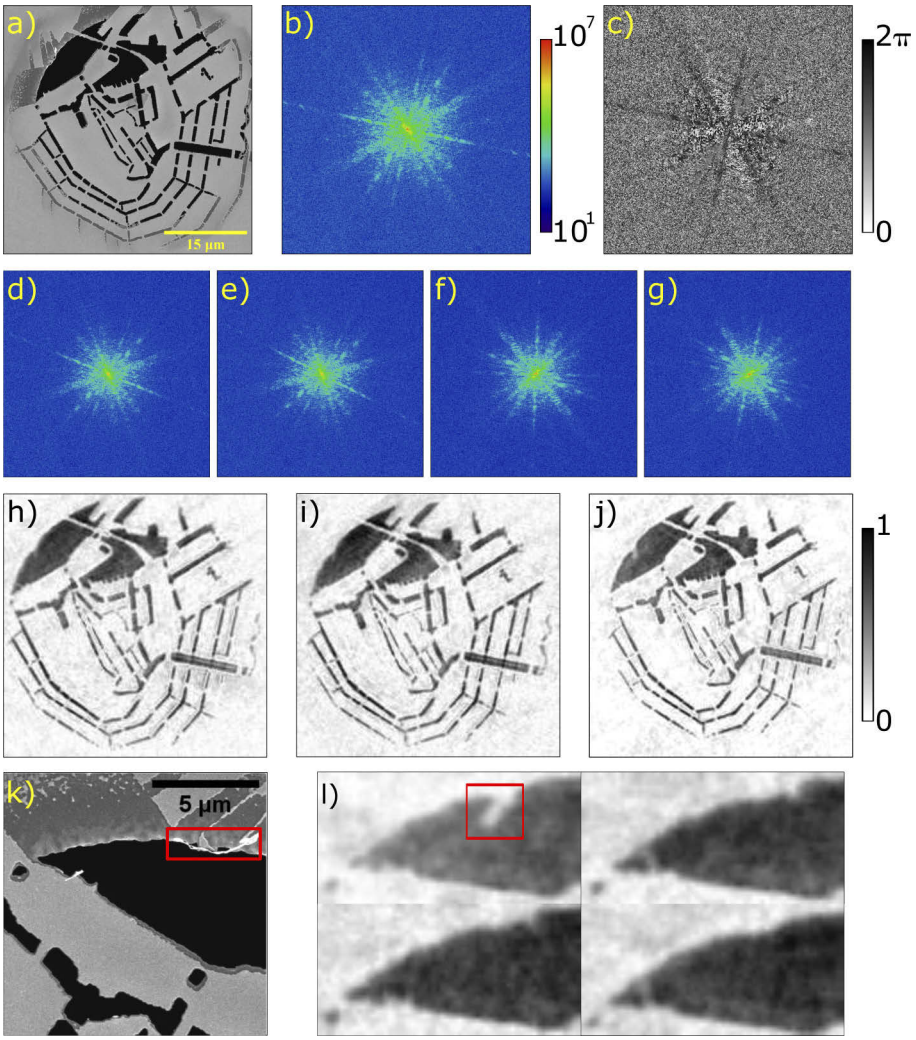

Fig. 4. Object reconstructions from experimental data using rotational DSI at a wavelength of 31 nm. a) SEM image of the transmission sample. b,c) Intensity (log-scale) and phase of the diffraction pattern at 31 nm wavelength, obtained from the FTS scan at 0 degree angle. d-g) Diffraction intensity (log-scale) measured at 10, 15, 80 and 90 degree sample orientation. h-j) Object images obtained from the DSI reconstruction when including measurements at three, four and five different angles, respectively. k) Close-up of the SEM image highlighting a small contamination that moved upon rotation. l) Close-up of the reconstructed images at sample orientations at 0° (top left), 10°, 15° and 90° (bottom right), showing how the contamination is reconstructed differently at these different angles.

a more monotonous fashion. The results of these reconstructions when including three, four and five angles are displayed in Figs. 4(h)–4(j), respectively. For the three- and four-angle reconstructions, the quality of the results was consistently good if a sufficiently large angular range (i.e. 0-90°) is included. In all reconstructions, the estimated resolution is 300 nm, based on the size of the smallest resolved features. This resolution matches well with the highest spatial frequency that was detected above the noise level. When comparing the reconstructions for the different number of included angles, we find that the resolution is similar between all

Optics EXPRESS

reconstructions. The reconstructed image for five angles does show slightly sharper edges with less residual ripples in most parts of the image, but a consistent and significant resolution improvement cannot be claimed. Slight improvements can also be seen in the contrast of the images when including more angles. This mainly appears as a more homogeneous intensity distribution in the larger spaces (both light and dark), as well as in a more accurate representation of the partially transmitting areas. From these results we conclude that the main improvement in diversity from the rotational DSI approach is reached upon inclusion of data from at least three angles, and that adding data taken at more angles only results in moderate further improvements.

A noteworthy aspect in the retrieved object images, is that the algorithm is robust against some variation in the actual object upon rotation. It was found that the fabricated sample contained a small contamination that was loosely attached to an edge of a larger open area, and that this feature changed its orientation as the sample was rotated over 90°. An zoomed-in SEM image showing this contamination is displayed in Fig. 4(k). The rotational DSI algorithm calculates an average field estimate in each update step. Nevertheless, when the final field estimate is calculated using the averaged phase combined with the diffraction intensity from a specific rotation angle, images are obtained that show variations in the location of the contamination, in a way that matched the expectation for how this feature would move upon rotation when considering gravity. Parts of the reconstructions for 0°, 10°, 15° and 90° highlighting this contamination are shown in Fig. 4(l). It should however be noted that, although the reconstruction is robust against real object variations between measurements at different angles, the presence of such changes does violate a basic assumption of the algorithm. Although the contamination observed here was too small a detail to limit reconstruction quality, the robustness to such variations is still a subject of further study.

5. Conclusion

We have demonstrated that using rotational diversity in combination with an asymmetric probe beam enables CDI image reconstruction without prior knowledge about the object support, other than that the object is contained within the imaging field-of-view. We have experimentally verified this concept, using the DSI approach that we developed earlier, in which interference between two coherent extreme-ultraviolet beams results in the asymmetric probe beam structure. We find that, although in principle the concept works with diffraction patterns recorded at only two angles, the inclusion of data for up to five different angles results in improved image quality and more robust reconstruction. The developed method provides a convenient way of relaxing support constraint requirements and/or other forms of prior knowledge in CDI, and enables robust reconstruction using only a limited number of measured diffraction patterns.

Funding

European Research Council (ERC-StG 637476); Nederlandse Organisatie voor Wetenschappelijk Onderzoek.

Acknowledgments

This work has been carried out at ARCNL, a public-private partnership of UvA, VU, NWO and ASML.

References

1. H. N. Chapman and K. A. Nugent, "Coherent lensless X-ray imaging," Nat. Photonics **4**(12), 833–839 (2010).
2. D. Shapiro, P. Thibault, T. Beetz, V. Elser, M. Howells, C. Jacobsen, J. Kirz, E. Lima, H. Miao, A. M. Neiman, and D. Sayre, "Biological imaging by soft x-ray diffraction microscopy," Proc. Natl. Acad. Sci. U. S. A. **102**(43), 15343–15346 (2005).

Optics EXPRESS

3. M. Holler, M. Guizar-Sicairos, E. H. R. Tsai, R. Dinapoli, E. Müller, O. Bunk, J. Raabe, and G. Aeppli, "High-resolution non-destructive three-dimensional imaging of integrated circuits," Nature **543**(7645), 402–406 (2017).
4. M. Zürch, J. Rothhardt, S. Hädrich, S. Demmler, M. Krebs, J. Limpert, A. Tünnermann, A. Guggenmos, U. Kleineberg, and C. Spielmann, "Real-time and Sub-wavelength Ultrafast Coherent Diffraction Imaging in the Extreme Ultraviolet," Sci. Rep. **4**(1), 7356 (2015).
5. Y. Jiang, Z. Chen, Y. Han, P. Deb, H. Gao, S. Xie, P. Purohit, M. W. Tate, J. Park, S. M. Gruner, V. elser, and D. A. Muller, "Electron ptychography of 2D materials to deep sub-ångström resolution," Nature **559**(7714), 343–349 (2018).
6. R. A. Bartels, A. Paul, H. Green, H. C. Kapteyn, M. M. Murnane, S. Backus, I. P. Christov, Y. Liu, D. Attwood, and C. Jacobsen, "Generation of Spatially Coherent Light at Extreme Ultraviolet Wavelengths," Science **297**(5580), 376–378 (2002).
7. D. F. Gardner, M. Tanksalvala, E. R. Shanblatt, X. Zhang, B. R. Galloway, C. L. Porter, R. Karl Jr, C. Bevis, D. E. Adams, H. C. Kapteyn, M. M. Murnane, and G. F. Mancini, "Subwavelength coherent imaging of periodic samples using a 13.5 nm tabletop high-harmonic light source," Nat. Photonics **11**(4), 259–263 (2017).
8. G. S. M. Jansen, A. C. C. de Beurs, X. Liu, K. S. E. Eikema, and S. Witte, "Diffractive shear interferometry for extreme ultraviolet high-resolution lensless imaging," Opt. Express **26**(10), 12479 (2018).
9. S. Witte, V. T. Tenner, D. W. E. Noom, and K. S. E. Eikema, "Lensless diffractive imaging with ultra-broadband table-top sources: from infrared to extreme-ultraviolet wavelengths," Light: Sci. Appl. **3**(3), e163 (2014).
10. Y. Meng, C. Zhang, C. Marceau, A. Yu. Naumov, P. B. Corkum, and D. M. Villeneuve, "Octave-spanning hyperspectral coherent diffractive imaging in the extreme ultraviolet range," Opt. Express **23**(22), 28960 (2015).
11. B. Zhang, D. F. Gardner, M. H. Seaberg, E. R. Shanblatt, C. L. Porter, R. Karl, C. A. Mancuso, H. C. Kapteyn, M. M. Murnane, and D. E. Adams, "Ptychographic hyperspectral spectromicroscopy with an extreme ultraviolet high harmonic comb," Opt. Express **24**(16), 18745 (2016).
12. J. Miao, P. Charalambous, J. Kirz, and D. Sayre, "Extending the methodology of X-ray crystallography to allow imaging of micrometre-sized non-crystalline specimens," Nature **400**(6742), 342–344 (1999).
13. J. R. Fienup, "Reconstruction of an object from the modulus of its Fourier transform," Opt. Lett. **3**(1), 27 (1978).
14. V. T. Tenner, K. S. E. Eikema, and S. Witte, "Fourier transform holography with extended references using a coherent ultra-broadband light source," Opt. Express **22**(21), 25397 (2014).
15. S. Marchesini, H. He, H. N. Chapman, S. P. Hau-Riege, A. Noy, M. R. Howells, U. Weierstall, and J. C. H. Spence, "X-ray image reconstruction from a diffraction pattern alone," Phys. Rev. B **68**(14), 140101 (2003).
16. J. M. Rodenburg and H. M. L. Faulkner, "A phase retrieval algorithm for shifting illumination," Appl. Phys. Lett. **85**(20), 4795–4797 (2004).
17. P. Thibault, M. Dierolf, A. Menzel, O. Bunk, C. David, and F. Pfeiffer, "High-Resolution Scanning X-ray Diffraction Microscopy," Science **321**(5887), 379–382 (2008).
18. G. S. M. Jansen, D. Rudolf, L. Freisem, K. S. E. Eikema, and S. Witte, "Spatially resolved Fourier transform spectroscopy in the extreme ultraviolet," Optica **3**(10), 1122 (2016).
19. D. R. Austin, T. Witting, C. A. Arrell, F. Frank, A. S. Wyatt, J. P. Marangos, J. W. G. Tisch, and I. A. Walmsley, "Lateral shearing interferometry of high-harmonic wavefronts," Opt. Lett. **36**(10), 1746 (2011).
20. H. Wang, C. Liu, X. Pan, J. Cheng, and J. Zhu, "Phase imaging with rotating illumination," Chin. Opt. Lett. **12**(1), 010501 (2014).
21. D. E. Boonzajer Flaes and S. Witte, "Interference probe ptychography for computational amplitude and phase microscopy," Opt. Express **26**(24), 31372 (2018).
22. C. Falldorf, C. von Kopylow, and R. B. Bergmann, "Wave field sensing by means of computational shear interferometry," J. Opt. Soc. Am. A **30**(10), 1905 (2013).
23. I. Harder, J. Schwider, and N. Lindlein, "DUV-shearing interferometer with reduced spatial coherence," DGaO Proc. **106**, A11 (2005).
24. T. Weitkamp, A. Diaz, C. David, F. Pfeiffer, M. Stampanoni, P. Cloetens, and E. Ziegler, "X-ray phase imaging with a grating interferometer," Opt. Express **13**(16), 6296 (2005).
25. S. Marchesini, "Invited article: A unified evaluation of iterative projection algorithms for phase retrieval," Rev. Sci. Instrum. **78**(1), 011301 (2007).
26. K. G. Larkin, M. Oldfield, and H. Klemm, "Fast Fourier method for the accurate rotation of sampled images," Opt. Commun. **139**(1-3), 99–106 (1997).
27. J. R. Fienup, "Invariant error metrics for image reconstruction," Appl. Opt. **36**(32), 8352 (1997).